HIGH-TIME-RESOLUTION MEASUREMENTS OF THE POLARIZATION OF THE CRAB PULSAR AT 1.38 GHz

AGNIESZKA SŁOWIKOWSKA[1], BENJAMIN W. STAPPERS[2], ALICE K. HARDING[3], STEPHEN L. O'DELL[4],
RONALD F. ELSNER[4], ALEXANDER J. VAN DER HORST[5], AND MARTIN C. WEISSKOPF[4]

[1] Kepler Institute of Astronomy, University of Zielona Góra, Lubuska 2, 65-265 Zielona Góra, Poland
[2] Jodrell Bank Centre for Astrophysics, University of Manchester, Manchester M13 9PL, UK
[3] Astrophysics Science Division, NASA Goddard Space Flight Center, Greenbelt, MD 20771, USA
[4] Astrophysics Office, NASA Marshall Space Flight Center, ZP12, Huntsville, AL 35812, USA
[5] Astronomical Institute, University of Amsterdam, Science Park 904, 1098 XH Amsterdam, The Netherlands
Received 2014 February 27; accepted 2014 November 9; published 2015 January 15

ABSTRACT

Using the Westerbork Synthesis Radio Telescope, we obtained high-time-resolution measurements of the full polarization of the Crab pulsar. At a resolution of 1/8192 of the 34 ms pulse period (i.e., 4.1 μs), the 1.38 GHz linear-polarization measurements are in general agreement with previous lower-time-resolution 1.4 GHz measurements of linear polarization in the main pulse (MP), in the interpulse (IP), and in the low-frequency component (LFC). We find the MP and IP to be linearly polarized at about 24% and 21% with no discernible difference in polarization position angle. However, contrary to theoretical expectations and measurements in the visible, we find no evidence for significant variation (sweep) in the polarization position angle over the MP, the IP, or the LFC. We discuss the implications, which appear to be in contradiction to theoretical expectations. We also detect weak circular polarization in the MP and IP, and strong ($\approx$20%) circular polarization in the LFC, which also exhibits very strong ($\approx$98%) linear polarization at a position angle of 40° from that of the MP or IP. The properties are consistent with the LFC, which is a low-altitude component, and the MP and IP, which are high-altitude caustic components. Current models for the MP and IP emission do not readily account for the absence of pronounced polarization changes across the pulse. We measure IP and LFC pulse phases relative to the MP consistent with recent measurements, which have shown that the phases of these pulse components are evolving with time.

Key words: polarization – pulsars: general – pulsars: individual (Crab: PSR B0531+21) – stars: neutron

1. INTRODUCTION

The Australia Telescope National Facility Pulsar Catalog (Manchester et al. 2005) lists over 2300 radio pulsars. Several radio studies (e.g., Gould & Lyne 1998; Karastergiou & Johnston 2006; Weltevrede & Johnston 2008) have measured the polarization for many of these pulsars. Radio pulsars typically show moderate-to-strong linear polarization (p_L), which is stronger for those of higher spin-down energy-loss rates (Weltevrede & Johnston 2008, Figure 8). The linear polarization sometimes exhibits a characteristic swing or sweep of the position angle in an S-like shape near the pulse center, which is routinely interpreted in terms of the rotating vector model (Radhakrishnan & Cooke 1969). For this model, the point of emission is assumed to be in the polar cap region of the pulsar where a dipolar magnetic-field line points with a small angle (beamwidth) toward the observer. The two free parameters of this simple model are the angle between the axes of rotation and the orientation of the magnetic dipole, and the view angle between the line of sight and the rotation axis. The variation of the radio position angle from some pulsars (e.g., Lyne & Graham-Smith 2006, and references therein) can be described by this model.

The Crab pulsar, the compact remnant of SN1054, and its pulsar wind nebula (PWN) are among the most intensively studied objects in the sky. The pulsar is one of the youngest and most energetic and its pulsed emission has been detected from 10 MHz (Bridle 1970) up to 400 GeV by VERITAS (Aliu et al. 2011) and MAGIC (Aleksić et al. 2012). The PWN is detected at energies up to 100 TeV (Aharonian et al. 2004, 2006; Allen & Yodh 2007; Abdo et al. 2012). Both the pulsar and nebula are predominantly sources of non-thermal radiation (synchrotron, curvature, and Compton processes), indicated not only by the broadband spectral continua, but also by strong polarization in many wavelength bands (Lyne & Graham-Smith 2006; Bühler & Blandford 2014).

In the visible band, spatially resolved polarimetry of the nebula, which began over a half century ago (Oort & Walraven 1956; Woltjer 1957), continues (e.g., Moran et al. 2013b, and references therein). Owing to its brightness, phase-resolved optical polarimetry of the pulsar has also been possible (Jones et al. 1981; Smith et al. 1988; Słowikowska et al. 2009). However, phase-resolved X- and γ-ray polarimetry measurements of the Crab pulsar require space-based instruments, which have had limited sensitivity. OSO-8 observations (Silver et al. 1978) of the Crab only established upper limits to the X-ray (2.6 keV and 5.2 keV) polarization of the pulsed emission. INTEGRAL IBIS observations (Forot et al. 2008; Moran et al. 2013a) also detect no significant pulsed γ-ray (200–800 keV) polarization, although the off-pulse emission appears highly linearly polarized and is possibly associated with structures close to the pulsar rather than with the pulsar itself.

The Crab pulsar's light curve exhibits different features at different wavelengths, but it is currently the only pulsar for which the principal features persist over all wavelengths, from radio to γ-ray. There are two principal components—the main pulse (MP) and the interpulse (IP). This double-peak structure remains more-or-less phase-aligned over all spectral bands (Moffett & Hankins 1996; Kuiper et al. 2001). One of several additional features in the radio band is the low-frequency component (LFC; e.g., Moffett & Hankins 1996, 1999), which has a very low amplitude and occurs at $\approx$0.10 of the fractional

pulse phase ($36°$) before the MP. This component is most prominent around 1.4 GHz, in contrast with the "precursor" component (Moffett & Hankins 1996), which precedes the MP by ≈ 0.05 of the fractional pulse phase ($19°$) at 0.327 and 0.610 GHz (Table 2 of Backer et al. 2000).

The MP and IP appear at roughly the same pulse phase from radio to γ-ray wavelengths, suggesting that their emission originates from a similar location in the magnetosphere at all wavebands. Modeling of γ-ray light curves from the many pulsars observed by the *Fermi Gamma-ray Space Telescope* (Abdo et al. 2013) strongly indicates that the high-energy emission originates in the outer magnetosphere, at altitudes comparable to the light-cylinder radius (Romani & Watters 2010; Pierbattista et al. 2014; Bai & Spitkovsky 2010). Outer magnetosphere emission models, such as the outer-gap (Romani & Yadigaroglu 1995), slot-gap (Muslimov & Harding 2004), and current-sheet (Pétri & Kirk 2005) had been proposed and studied prior to the *Fermi* observations, but their emission geometry seems to account for the characteristics and variety of observed γ-ray light curves. In addition, *Fermi* has discovered a number of γ-ray millisecond pulsars whose radio peaks are nearly aligned with their γ-ray peaks (e.g., Espinoza et al. 2013), like the Crab. Modeling both γ-ray and radio light curves of these pulsars with the same outer magnetosphere emission models used to model young pulsars has suggested that their radio emission may originate from very high altitudes (Venter et al. 2012). Thus, in this paper, we compare the phase-resolved radio polarization observations (Section 2) that we have analyzed (Section 3) with such models (Section 4).

Manchester (1971) measured the linear polarization of the Crab pulsar's MP and precursor components at two radio frequencies. The 0.410 GHz measurements found the MP to be 20% linearly polarized at position angle $140°$ and the precursor to be 80% linearly polarized at A position angle of $140°$. The 1.664 GHz measurements found the MP to be 24% linearly polarized at a position angle of $60°$ and the precursor to be completely absent. As these measurements had rather large uncertainties and were obtained with a time resolution 1/256 of the pulse period, they were quite limited for detecting variation of the linear polarization degree or position angle within a feature. However, Manchester noted a suggestion of rotation of the 1.664 GHz polarization position angle by about $30°$ through the MP.

More recently, Moffett & Hankins (1999) examined the pulse-profile morphology and polarization properties at three radio frequencies—1.424 GHz, 4.885 GHz, and 8.435 GHz—with a time resolution of $256\,\mu s$ (about 1/130 of the pulse period). The 1.424 GHz measurements found the MP to be 25% linearly polarized at a position angle of $120°$; the IP, 20% at position angle of $120°$; and the LFC, 45% at a position angle of $155°$. Moffett & Hankins note that the polarization position angle "changes across the full period, although not significantly within components."

Here we first report our observations (Section 2), using the Westerbork Synthesis Radio Telescope (WSRT) in the Netherlands, of the full (linear and circular) 1.38 GHz polarization of the Crab pulsar, at high time resolution. We then describe the polarimetry analysis and results (Section 3 and Appendix) for the three pulse components, with a primary objective of determining the sweep of the position angle across each. Next, we discuss the implications (Section 4) of our measurements and analysis upon theoretical models for the pulsar emission. Finally, we summarize our conclusions (Section 5).

2. THE OBSERVATIONS

The WSRT observations, on 2011 August 8, used 14 25 m diameter dishes combined coherently to form the equivalent of a 94 m dish for pulsar observations. Owing to the interferometric nature of the WSRT, the observations partially resolve out the radio-bright Nebula, thus improving sensitivity over typical single-dish observations. Moreover, as the WSRT is an equatorially mounted telescope, there is no need to correct for the parallactic angle.

To coherently combine the dishes, correlated data from observations of a bright calibrator source are used to determine phase delays among dishes. This is initially accomplished using an unpolarized calibrator to determine delays between the two linear polarizations separately, followed by the observation of a polarized calibrator to determine any residual delays between the two polarizations. These procedures accurately calibrate the relative fluxes in the four Stokes parameters—hence, the polarization properties—but not the absolute flux. Consequently, we express the Stokes measurements (e.g., Figure 1) in arbitrary units.

The PuMa-II (Karuppusamy et al. 2008) pulsar back end was used to record Nyquist-sampled voltages at 8 bit resolution, across a 160 MHz band centered on 1380 MHz, for PSRs B0531+21 (Crab) and B0355+54, for a total of 144 and 18 minutes, respectively. The data were subsequently coherently de-dispersed and folded using the DSPSR (van Straten & Bailes 2011) software package. Polarization profiles were formed after correcting for (frequency-dependent) interstellar Faraday rotation (rotation measure RM $= -42.3 \pm 0.5$ rad m^{-2}) of the position angle, using the PSRCHIVE software package (van Straten et al. 2012). The polarization calibration was already carried out when forming the coherent sum of the dishes; nevertheless, PSR B0355+54 was observed to verify that no further polarization calibration was required. Comparison with the profile observed by Gould & Lyne (1998) showed that the polarization calibration matched exactly. The Crab–pulsar profile was folded using the Jodrell Bank Ephemeris[6] with 8192 bins (about 4.1 μs/bin) across the pulse profile, matching the time resolution of the data after dividing into frequency channels and coherently de-dispersing. This time resolution was also chosen to approximately match the minimum broadening caused by scattering of the Crab pulsed emission by free electrons in the Crab Nebula (e.g., Backer et al. 2000; Kuzmin et al. 2008).

Figure 1 displays our measurement of the four Stokes parameters I, Q, U, and V—which fully characterize the polarization—folded on the pulse period. Unfortunately, we were unable to determine the absolute polarization position angle for the Crab pulsar observation. Instead, we selected a coordinate system for the Stokes parameters such that the MP has $U = 0$ and $Q < 0$. Inspection of Figure 1 immediately shows that our 1.38 GHz observations detect the flux and polarization of three components—MP, IP, and LFC. Like the MP, the IP has $U \approx 0$ and $Q < 0$; but the LFC has $U < 0$ and $Q \approx 0$: Thus, the polarization position angles for the MP and the IP are roughly equal but differ from that of the LFC by about $40°$ (see Equation (2)). Similarly, but less obviously, the circular polarization of the MP and the IP are comparable, but that of the LFC has opposite polarity.
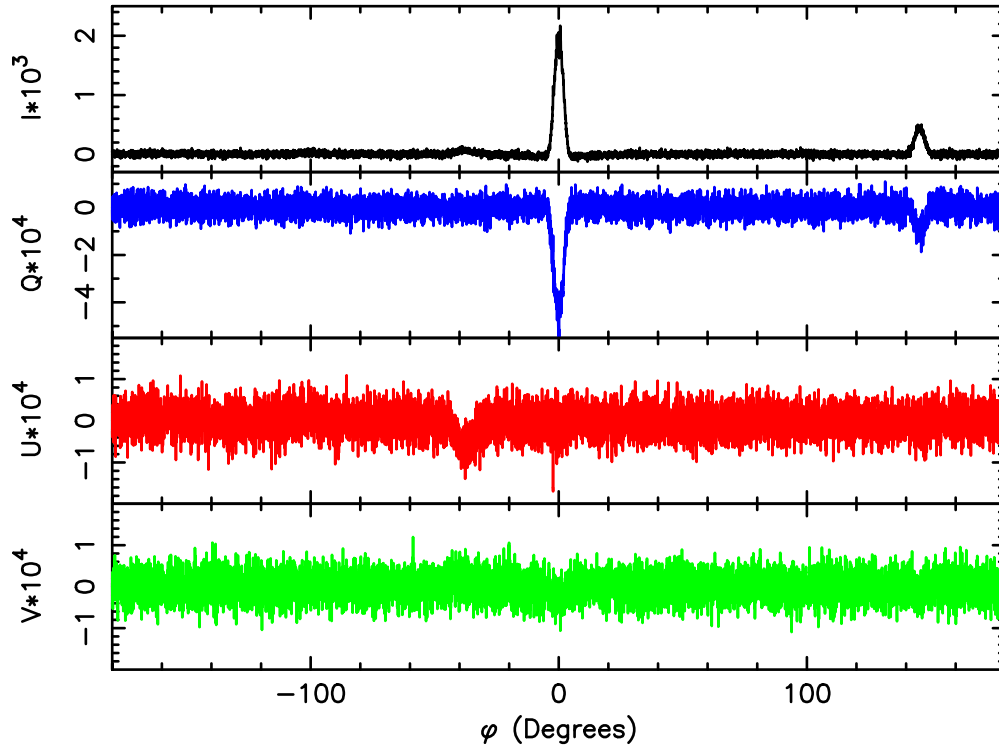
---

[6] http://www.jb.man.ac.uk/pulsar/crab.html

Figure 1. Four Stokes parameters $I \times 10^3$, $Q \times 10^4$, $U \times 10^4$, and $V \times 10^4$ (arbitrary units) as functions of pulse phase φ, where the peak of the main pulse (MP) defines $\varphi = 0$. The coordinate system for the Stokes parameters here sets $U = 0$ and $Q < 0$ for the MP.

3. ANALYSIS AND RESULTS

The Stokes parameters have several virtues: they are statistically independent, typically exhibit Gaussian errors, and are directly superposable—i.e., each Stokes component (I, Q, U, or V) for multiple sources is the sum of the respective Stokes component for each source. These properties follow from the fact that the Stokes parameters describe the polarization state in Cartesian-like coordinates. This has the added virtue that there is no coordinate singularity at the origin, as occurs for polar-like coordinates—such as the linear-polarization degree p_L and position angle ψ. Consequently, we perform all statistical analyses and model fitting (Appendix) on (pre-processed, Appendix A.1) raw Stokes data.

It is, of course, straightforward to transform to more customary parameters—e.g., linear-polarization degree p_L (Equation (1)), position angle ψ (Equation (2)), and circular-polarization (signed) degree p_C (Equation (3)):

$$p_L = \sqrt{(Q^2 + U^2)}/I; \qquad (1)$$

$$\psi = \frac{1}{2}\tan^{-1}(U/Q); \qquad (2)$$

$$p_C = V/I. \qquad (3)$$

For the three pulse features (MP, IP, and LFC), we estimate $p_L(\varphi_n)$, $\psi(\varphi_n)$, and $p_C(\varphi_n)$ at each datum n by substituting the measured I_n, Q_n, U_n, and V_n into Equations (1), (2), and (3).

Figures 2 and 3 display the direct estimates of I_n, p_{Ln}, ψ_n, and p_{Cn} over the MP and IP, respectively. As the LFC is quite weak relative to the MP and the IP, the plots for the LFC are too noisy to display legibly. Even for the stronger features—MP and IP—the rms noise in the directly calculated polarization parameters (p_{Ln}, ψ_n, and p_{Cn}), which serve as estimators of the statistical error, substantially increases away from the pulse center due to the low signal-to-noise ratio *per sample* in the pulse wings. In order to deal effectively with low-signal-to-noise data in the wings of the MP and IP and throughout the (weaker) LFC, we adopt a more rigorous forward-modeling approach to fit the measured Stokes data to the modeled $I(\varphi)$, $Q(\varphi)$, $U(\varphi)$, and $V(\varphi)$:

$$Q(\varphi) = I(\varphi) p_L(\varphi) \cos(2\psi(\varphi)); \qquad (4)$$

$$U(\varphi) = I(\varphi) p_L(\varphi) \sin(2\psi(\varphi)); \qquad (5)$$

$$V(\varphi) = I(\varphi) p_C(\varphi). \qquad (6)$$

Appendix describes in some detail our approach for fitting polarization models to the Stokes data. As Figures 2 and 3 indicate that neither $p_L(\varphi)$, $\psi(\varphi)$, nor $p_C(\varphi)$ vary rapidly across the pulse profile, the approach simply models $p_L(\varphi)$, $\psi(\varphi)$, and $p_C(\varphi)$ as Taylor-series expansions in the phase-angle offset $\Delta\varphi \equiv (\varphi - \varphi_0)$ from the center φ_0 of the respective pulse feature (MP, IP, or LFC). Table 1 tabulates the best-fit Taylor-expansion coefficients for the polarization dependence upon the phase-angle offset:

$$p_L(\varphi) = p_{L0} + p'_{L0}(\varphi - \varphi_0) + \frac{1}{2}p''_{L0}(\varphi - \varphi_0)^2; \qquad (7)$$

$$\psi(\varphi) = \psi_0 + \psi'_0(\varphi - \varphi_0) + \frac{1}{2}\psi''_0(\varphi - \varphi_0)^2; \qquad (8)$$

$$p_C(\varphi) = p_{C0} + p'_{C0}(\varphi - \varphi_0) + \frac{1}{2}p''_{C0}(\varphi - \varphi_0)^2. \qquad (9)$$

An important conclusion of this study is that the Stokes data are consistent—within statistical uncertainties—with constant
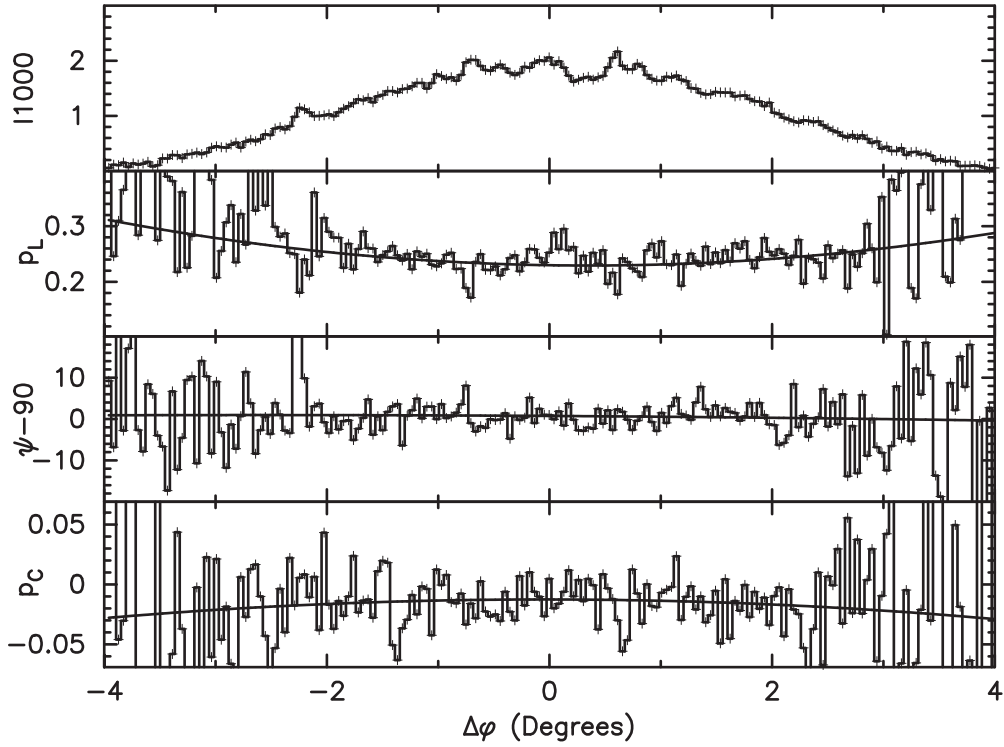
Figure 2. Direct estimate of customary polarization parameters of the main pulse vs. the phase-angle offset $\Delta\varphi$ from the MP center. From the top, the plots display measured intensity I data and then directly calculated fractional linear polarization p_L, position angle ψ, and fractional circular polarization p_C. The smooth solid lines show the best-fit phase-dependent polarization properties based upon forward modeling of the Stokes data (Table 1).
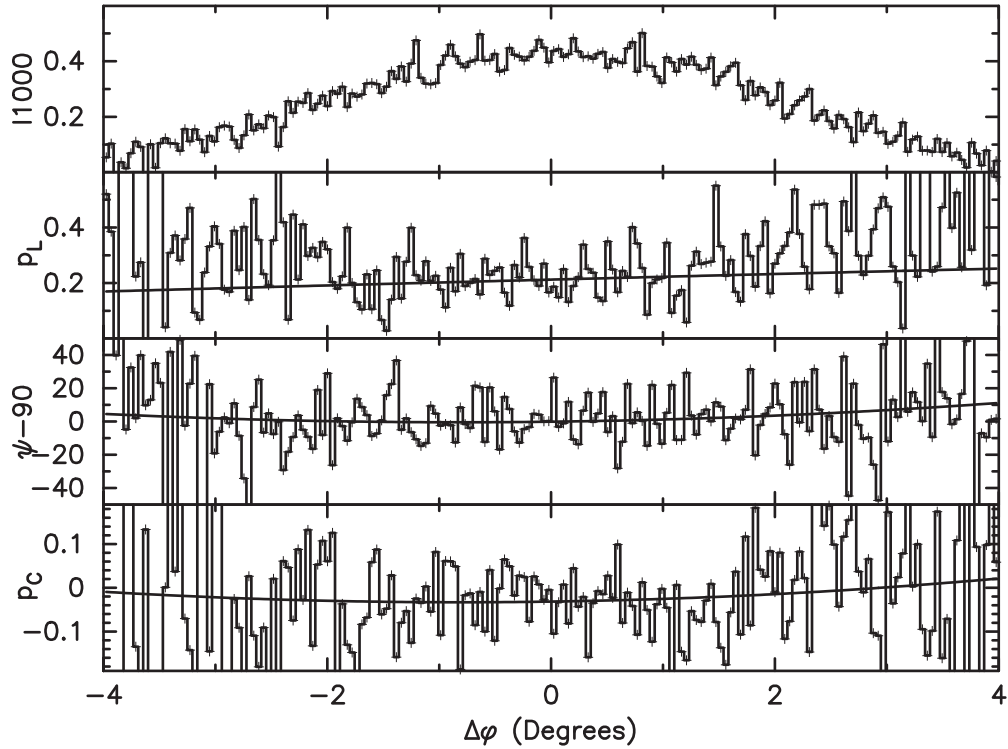

Figure 3. Direct estimate of customary polarization parameters of the interpulse vs. the phase-angle offset $\Delta\varphi$ from the IP center. From the top, the plots display measured intensity I data and then directly calculated fractional linear polarization p_L, position angle ψ, and fractional circular polarization p_C. The smooth solid lines show the best-fit phase-dependent polarization properties based upon forward modeling of the Stokes data (Table 1).

polarization position angle ψ across each of the three pulse features (MP, IP, and LFC) individually. However, the MP does exhibit a small but statistically significant quadratic variation in the linear-polarization degree p_L. While our 1.380 GHz

polarimetry of the Crab pulsar has finer time resolution and better statistical accuracy than previous 1.424 GHz polarimetry (Moffett & Hankins 1999), measured values for the polarization degree and position angle (relative to MP) are mostly similar
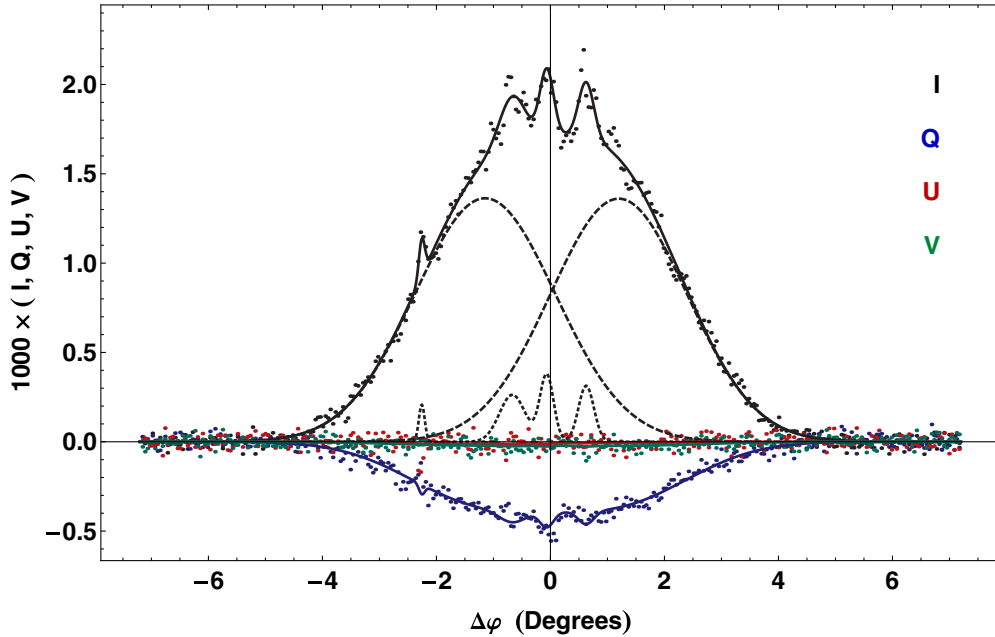
Figure 4. Stokes data I, Q, U, and V vs. pulse phase offset $\Delta\varphi$ from the center of the main pulse (MP). The lines represent the best-fit (minimum-χ^2) Stokes functions for a multi-Gaussian profile and up-to-second-order variations in linear-polarization degree, position angle, and circular-polarization degree. The pulse profile comprises 2 broad and 4 narrow Gaussians.

Table 1
Best-fit Polarization Coefficients for the MP, IP, and LFC, Using a Single
Gaussian for Each Pulse Profile and Up-to-quadratic Variations
in Polarization Functions $p_L(\varphi)$, $\psi(\varphi)$, and $p_C(\varphi)$

Parameter	Units	MP	IP	LFC
$\varphi_0 - \varphi_{\rm MP}$	°	$\equiv 0$	145.389 ± 0.027	-37.75 ± 0.19
p_{L0}	%	22.98 ± 0.30	21.3 ± 1.0	98.2 ± 6.7
p'_{L0}	%/°	-0.31 ± 0.19	1.02 ± 0.62	-0.8 ± 2.2
p''_{L0}	%/°/°	0.88 ± 0.22	-0.02 ± 0.63	0.0 ± 1.3
$\psi_0 - \psi_{\rm MP}$	°PA	$\equiv 0$	-0.1 ± 1.3	40.8 ± 1.5
ψ'_0	°PA/°	-0.16 ± 0.20	0.82 ± 0.78	-0.16 ± 0.49
ψ''_0	°PA/°/°	-0.06 ± 0.21	1.00 ± 0.89	-0.21 ± 0.28
p_{C0}	%	-1.25 ± 0.20	-3.15 ± 0.94	20.5 ± 4.9
p'_{C0}	%/°	0.01 ± 0.13	0.38 ± 0.56	0.3 ± 1.7
p''_{C0}	%/°/°	-0.20 ± 0.15	0.47 ± 0.57	-0.49 ± 0.97

for the MP and for the IP. The only significant difference is for the LFC's linear polarization degree and position angle. We measured nearly total (98% ± 7%) linear polarization at a +40°.8 ± 1°.5 position-angle offset from the MP, whereas Moffett & Hankins (1999) found the LFC to be ≈40% linearly polarized at an ≈ +30° position-angle offset from the MP. We also detect circular polarization, which is moderately strong in the LFC (20.5% ± 4.9%) but weak and of opposite polarity in the MP (−1.3% ± 0.2%) and in the IP (−3.2% ± 0.9%). In contrast with Moffett & Hankins, we find no significant variation in the circular polarization across any of the three pulse components MP, IP, and LFC.

Another important conclusion—albeit peripheral to the polarimetry—relates to substructure in the pulse profile of the MP. The fine time resolution and better statistical accuracy of our radio observation of the Crab pulsar resulted in measurement of statistically significant substructure (Appendix A.3) in the profile of the MP (Figure 4). The typical width of the substructure is roughly 10 μs—i.e., $\leqslant 0.1$ the width of the MP profile. As the current analysis utilizes the sum of all data collected

during the observation at a single epoch (2011 August 8), we have not assessed the temporal behavior of the profile. However, we presume that this substructure results from sporadic, very strong giant radio pulses (Bhat et al. 2008; Karuppusamy et al. 2010; Majid et al. 2011; Hankins et al. 2003) occurring during the 144 minute observation. Although the substructure is readily apparent in the I profile of the MP, the discernible subpulses contribute only about 5% of the fluence in the MP over the observation. However, they likely result from only the strongest giant radio pulses in a distribution of pulse amplitudes. Note that our conclusions as to the average pulse-phase dependences of the polarimetry are effectively independent of the precise modeling of the intensity profile of the MP. On the other hand, inspection of the Stokes parameters (Figure 4) or polarization parameters (Figure 2) indicates that the polarization of some of the subpulses (e.g., at phase offset $\Delta\varphi \approx -2°.3$) differs substantially from the average polarization of the MP.

We also note that our WSRT-measured pulse-phase offsets of the IP and of the LFC from the MP are in good agreement with contemporaneous measurements at the Jodrell Bank (Lyne et al. 2013). This tends to support the conclusion of Lyne et al. (2013) that the phase separations of the IP and of the LFC from the MP are evolving with time. Furthermore, the evolution of phase separations might contribute to the difference between our measurement of the LFC's polarization and earlier measurements (Moffett & Hankins 1999).

4. IMPLICATIONS FOR THEORETICAL MODELS

Emission at altitudes comparable to the light-cylinder radius produce caustic peaks, formed by the cancellation of phase differences due to aberration and retardation with that due to field-line curvature of radiation along the trailing magnetic-field lines (Dyks & Rudak 2003). In outer-magnetosphere models, peaks in the light curves form when the observer's sight line sweeps across one or more bright caustic. The caustics display distinct linear-polarization characteristics (Dyks et al. 2004),

including fast sweeps of position angle and dips in polarization degree at the peaks, which are caused by piling up radiation emitted over a large range of altitudes and magnetic-field directions into the caustics. These characteristics are in fact seen in the optical polarization of the Crab pulsar (Słowikowska et al. 2009), which exhibits rapid swings of position angle across both the MP and IP, as well as dips in the polarization degree to the 5% level on the trailing edge of each peak.

From the results presented in this paper, however, the characteristics of the radio linear polarization of the MP and IP resemble neither those of caustics in existing geometric models nor those observed in the optical emission. The lack of position-angle swing in the radio MP and IP is in stark contrast to the rapid position-angle swings in the optical. The very low circular polarization and moderate linear polarization observed here in the radio MP and IP are consistent with caustics, but the observed linear-polarization values ($\approx 22\%$) in the radio are significantly higher than those in the optical, and there is only a small variation with phase in the MP. On the other hand, the radio pulses are much narrower than the optical pulses, indicating that the radio MP and IP may originate along a smaller range of altitudes and/or in a subset of field lines.

We have modeled the caustic emission and corresponding linear-polarization degree p_L and position angle ψ for the Crab pulsar, with a simulation using geometric renditions of standard slot-gap and outer-gap emission. These geometric emission models assume constant emissivity in the corotating frame along a set of field lines within the gaps, defined by a gap width w across field lines in open-volume coordinates (Dyks et al. 2004), where the width is a fraction of radius of open magnetic field lines. As in Dyks et al. (2004), the emission is assumed to occur over a fixed radius range, from minimum $r_{\min}$ to maximum $r_{\max}$. For the simulations of Crab polarization here, we explored gap widths $w = 0.002, 0.01, 0.02, 0.05$, $r_{\min} = 0.3$–$0.9\,R_{\mathrm{LC}}$ and $r_{\max} = 0.5$–$1.2\,R_{\mathrm{LC}}$, where $R_{\mathrm{LC}} = c/\Omega$ is the light-cylinder radius. These are smaller ranges of altitude and smaller gap widths than in standard slot-gap or outer-gap models used in Dyks et al. (2004), which were $r_{\min} = R_{\mathrm{NS}}$, $r_{\max} = 0.95\,R_{\mathrm{LC}}$ for the slot gap and $r_{\min} = R_{\mathrm{NC}}$, $r_{\max} = 0.97\,R_{\mathrm{LC}}$ for the outer gap. Here R_{NS} is the neutron star radius and R_{NC} is the radius of the null-charge surface, at which the magnetospheric charge density in the corotating frame $\rho_0 = \mathbf{\Omega} \cdot \mathbf{B}/(2\pi c)$ vanishes.

We simulated emission using both retarded-vacuum-dipole (Deutsch 1955), as in Dyks et al. (2004), and force-free (Contopoulos & Kalapotharakos 2010) magnetic-field geometries, as in Harding et al. (2011). Then we computed light curves and Stokes parameters for magnetic inclination angles $\alpha = 45^\circ$–80°, with 5° resolution for vacuum and 15° resolution for force-free magnetospheres, and observer viewing angles $\zeta = 55^\circ$–80° (both with respect to the rotation axis). These ranges of α and ζ bracket the viewing angle of 60°–65° suggested by modeling of the X-ray torus (Ng & Romani 2008). Following Dyks et al. (2004), Blaskiewicz et al. (1991), and Hibschman & Arons (2001), we assume that the photon electric-field vector is parallel to the electron acceleration at each point along the field line to determine the Stokes parameters.

Although simulated light curves for the smaller gap widths produce narrower caustic peaks with less position-angle swing and depolarization, it is difficult to produce both $\psi(\varphi)$ and $p_L(\varphi)$ curves with no variation through the peaks. We compared a range of simulated light curves, p_L and ψ to the ones observed, and found that none of the models agree with the data. For the vacuum magnetospheres, the slot-gap model can produce

appropriately narrow peaks for $w < 0.01$, but there is always some change in ψ through both the MP and IP. At $\zeta = 60^\circ$, there are dips in p_L at only the first peak for $\alpha < 75^\circ$ and dips at both peaks for $\alpha > 75^\circ$. The outer-gap model produces a change in ψ mostly in the IP but dips in p_L in both peaks. While the force-free geometry, whose poloidal field lines are straighter than those in vacuum, can give a flatter position angle for certain inclination and viewing angles, the model's p_L shows strong variation through the peaks in contradiction with the data. For the force-free magnetospheres, the slot-gap model produces much less change in ψ at the peaks for $\zeta = 55^\circ$–65° and $\alpha = 45^\circ$–75°, but still not constant as observed. There is also a high level of depolarization in both peaks, but p_L is not constant through the peaks, as in the data. The outer gap in the force-free magnetosphere also produces changes in ψ and p_L in both peaks for these same ranges of α and ζ.

For comparison with our measurement of the phase-resolved polarization properties of the Crab pulsar, we simulated 66 total (48 vacuum and 18 force-free) cases. Based upon inspection of the results of these numerous simulated cases, the model light curve and polarization characteristics that seem to resemble most the Crab pulsar radio data is for the case of the slot-gap model in the force-free magnetosphere with $\alpha = 45^\circ$ and $\zeta = 60^\circ$. Figure 5 displays the results for this model for the MP. Note that this model does predict a rapid swing in polarization position angle and degree which we do not see; however, these swings occur on the preceding wing of the pulse, when the intensity is very low.

In order to explore the possibility that the linear-polarization degree p_L or position angle ψ changes sharply in the preceding wing of the MP (as in Figure 5), we fit the Stokes data to a simple model of a step jump in the values of p_L and of ψ at a pulse phase φ_{step}.

$$p_L(\varphi) = p_{L0} + \Delta p_L\, \Theta(\varphi_{\mathrm{step}} - \varphi); \qquad (10)$$

$$\psi(\varphi) = \psi_0 + \Delta\psi\, \Theta(\varphi_{\mathrm{step}} - \varphi). \qquad (11)$$

Here, p_{L0} and ψ_0 are the best-fit values for the constant linear-polarization degree and position angle; Δp_L and $\Delta\psi$, the pre-step differences in the value of each; and $\Theta(\varphi_{\mathrm{step}} - \varphi)$, the unit step distribution ($=1$ for $\varphi < \varphi_{\mathrm{step}}$, 0 otherwise). Figure 6 shows the best-fit differences and their (1-sigma) uncertainties as functions of pulse phase of the step (relative to pulse center). From this analysis, we conclude that any position-angle swing must be small—$|\Delta\psi| < 10^\circ$ for $\varphi_{\mathrm{step}} > -3^\circ.5$. A large position-angle swing—$|\Delta\psi| > 45^\circ$, say—is consistent with the data (but not required) only for $\varphi_{\mathrm{step}} < -4^\circ$. Note that the analysis requires $\Delta p_L > 0$ for $\varphi_{\mathrm{step}} \geqslant -2^\circ.5$ (and allows it for earlier φ_{step}), as this analysis does not include the small positive second derivative p_{L0}'' in the linear-polarization degree, which the Taylor-expansion fit to the MP Stokes data requires (see Table 1).

It is possible that the radio linear polarization in the MP and LP is very sensitive to the magnetic-field structure. Existing models explored only the two extremes of vacuum (accelerating fields but no plasma) and force-free (plasma but no accelerating fields), neither of which describe real pulsars. More realistic, dissipative magnetosphere models with finite conductivity now exist (Kalapotharakos et al. 2012; Li et al. 2012) and should be used to model light curves and polarization characteristics. It is also possible that the radio emission in the MP and IP occurs along sets of field lines that lie deeper within the
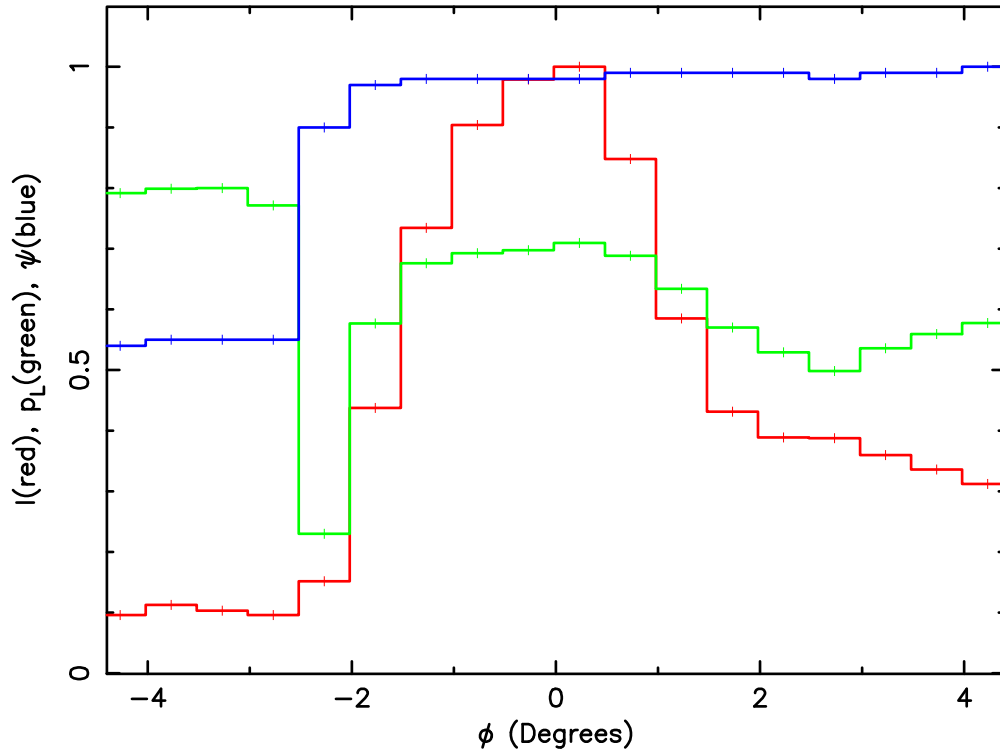
Figure 5. Predicted relative variation through the MP of the intensity I (red), linear polarization degree p_L (green), and position angle ψ (blue) for the slot-gap model, with a force-free magnetosphere. For this case, the magnetic inclination angle $\alpha = 45°$ and observer viewing angle $\zeta = 60°$ with respect to the spin axis. The ordinate range 0–1 corresponds to zero to peak intensity for I, 0%–100% polarization for p_L, and $-90°$ to $90°$ for ψ.
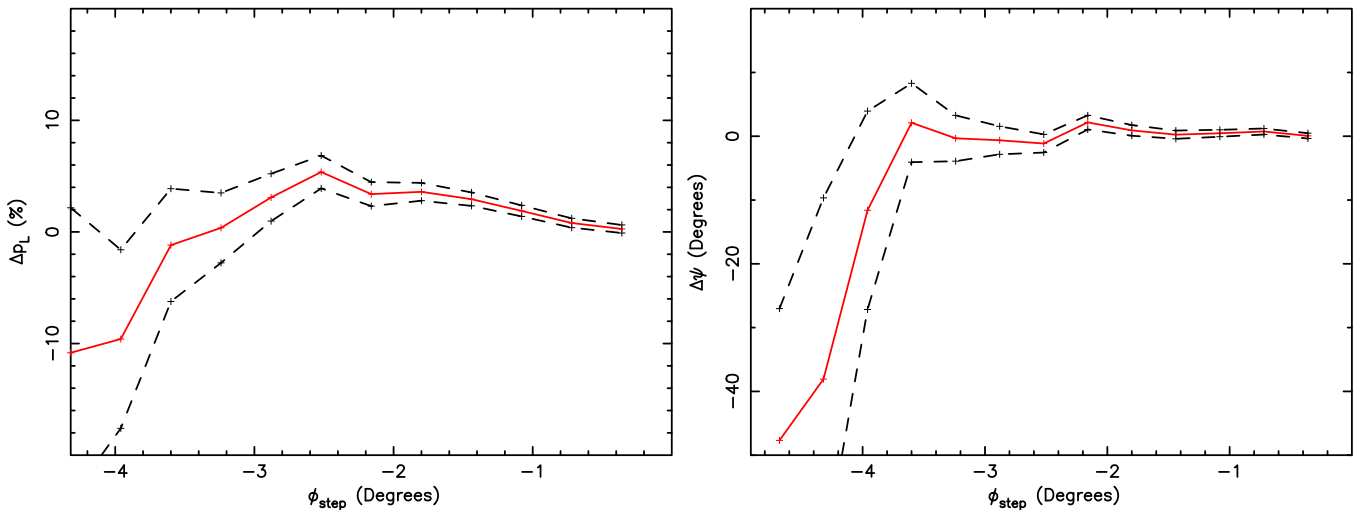

Figure 6. Constraints on a sharp step in the MP linear-polarization degree ($p_L(\varphi)$, left) and position angle ($\psi(\varphi)$, right) vs. the putative step's pulse phase φ_{step} (relative to the MP center). Large position-angle swings ($|\Delta\psi| > 45°$, say) are allowed (but not required) only very early ($\varphi_{step} < -4°$) in the pulse—i.e., where the signal-to-noise ratio is low.

open/closed field boundary or the current sheet and have different polarization properties.

The LFC is substantially weaker than the MP and IP at 1.4 GHz. As its name suggests, the LFC is not detected at radio frequencies higher than a few GHz and has no corresponding component in the visible band. The nearly complete radio polarization ($p_L \approx 98\%$ and $p_C \approx 20\%$) of the LFC support the hypothesis that it is a highly coherent, low-altitude component. Note that the (lower frequency) precursor is also believed to be a highly coherent, low-altitude component, due to its high polarization and steep spectrum (Rankin 1990).

5. CONCLUSIONS

Our 1.38 GHz observations of the Crab pulsar measured significant linear and circular polarization in the three most prominent pulse components—the MP, IP, and LFC. These results are mostly in agreement with previous measurements of linear polarization at similar radio frequencies (see Moffett & Hankins 1999). The MP and IP are moderately linearly polarized ($p_L \approx 23\%$ and 21%, respectively) at the same position angle ($\psi_{IP} - \psi_{MP} \approx 0$); they are weakly circularly polarized ($p_C \approx -1.3\%$ and -3.2%, respectively). In contrast, the LFC is very strongly linearly polarized ($p_L \approx 98\%$), at a

position angle $+40°$ from that of the MP or IP, and moderately circularly polarized ($p_C \approx 20\%$).

The fine time resolution (Period/8192 = 4.1 μs) and good sensitivity of the measurements at the WSRT enabled a meaningful search for changes in linear-polarization degree p_L, in position angle ψ, and in circular-polarization degree p_C across each of the three pulse components. Neither the MP, IP, nor LFC exhibits a statistically significant change in the polarization position angle or circular polarization across the pulse. For the MP, the linear term ("sweep") is well constrained: $\psi'_{0\,MP} = (−0.16 \pm 0.20)°PA/°$. Likewise, neither the IP nor LFC displays a statistically significant change in the polarization degree. However, the MP does show a small but statistically significant quadratic variation in linear-polarization degree—$p''_{L0\,MP} = (0.88 \pm 0.22)\%/°/°$ about its central value—$p_{L0\,MP} = (23.0 \pm 0.3)\%$—for a pulse-average linear polarization $\overline{p}_{L\,MP} = (23.7 \pm 0.3)\%$.

Our analysis of the radio Stokes data shows no strong sweep of the linear-polarization position angle. This lack of strong position-angle swings contrasts with the rapid swings observed in the visible band. Current models for pulsar emission geometries do not readily account for the absence of substantial variations in both polarization degree and position angle across a pulse component (Section 4). Thus, alternative models—e.g., dissipative magnetospheres—should be considered in modeling the radio polarization of the Crab pulsar's MP and IP. The nearly complete polarization of the LFC suggest that it originates at a different location and via a different mechanism than do the stronger MP and IP.

Finally, the fine time resolution and high signal-to-noise ratio in the MP data led to the detection of a statistically significant substructure in its pulse profile. We surmise that this substructure results from giant radio pulses occurring during the 144 minute observation.

APPENDIX

STATISTICAL ANALYSIS

A.1. Procedures

As Figure 1 shows, the main pulse (MP), interpulse (IP), and low-frequency component (LFC) are well separated in the 1.38 GHz data folded on the Crab pulsar's period. Consequently, we choose to analyze each of these three features individually, using phase ranges $(−7°.2, 7°.2)$ for the MP, $(134°.6, 156°.2)$ for the IP, and $(−52°.1, −23°.3)$ for the LFC, where the center of the MP defines pulse-phase angle $\varphi = 0°$. We use data over the remaining phase ranges to measure the off-pulse mean and the rms noise in I, Q, U, and V. Upon measuring the off-pulse mean values for I, we noticed that its off-pulse value near the

MP is depressed with respect to the remaining phase ranges. Specifically, in phase ranges $(−14°.4, −7°.2)$ and $(7°.2, 14°.4)$, the mean I is 0.0273 ($\times 1000$) less than in other off-pulse ranges. Taking this into account lowered χ^2 by about 300 in fitting the I pulse profile, but did not significantly alter the fitted polarization properties.

For convenience, we pre-process the raw data by subtracting the respective off-pulse mean value, under the assumption that the expectation values for I, Q, U, and V are zero away from pulse features. Furthermore, we take the RMS noise levels—0.0324, 0.0310, 0.0311, and 0.0307 (each $\times 1000$)—as estimators of the statistical standard deviations σ_I, σ_Q, σ_U, and σ_V, respectively.

In order to fit the model to the data for each pulse feature, we minimize the chi-square statistic of the combined Stokes data

$$
\begin{aligned}
\chi^2(\varpi) &= \chi^2_I(\varpi) + \chi^2_Q(\varpi) + \chi^2_U(\varpi) + \chi^2_V(\varpi) \\
&= \sum_{n=1}^{N} \left[\frac{(I_n - I(\varphi_n; \varpi))^2}{\sigma_I^2} + \frac{(Q_n - Q(\varphi_n; \varpi))^2}{\sigma_Q^2} \right. \\
&\quad \left. + \frac{(U_n - U(\varphi_n; \varpi))^2}{\sigma_U^2} + \frac{(V_n - V(\varphi_n; \varpi))^2}{\sigma_V^2} \right], \text{(A1)}
\end{aligned}
$$

with respect to a set ϖ of K model parameters, leaving $\nu = N − K$ degrees of freedom. We obtain the statistical uncertainty in each parameter, based upon $\Delta\chi^2 = \chi^2 − \chi^2_{\min}$. To perform the χ^2 analysis, we used the *Mathematica*™ (Wolfram Research, Inc 2013) function `NonlinearModelFit`,[7] which finds best-fit model parameters, their errors, correlation matrix among them, etc.

Modeling the Stokes data requires parameterized functions for the pulse profile $I(\varphi)$, the linear-polarization fraction $p_L(\varphi)$, the polarization position angle $\psi(\varphi)$, and the circular-polarization fraction $p_C(\varphi)$ (see Equations (4), (5), and (6) for $Q(\varphi)$, $U(\varphi)$, and $V(\varphi)$, respectively). As there is no evidence for rapid changes in polarization degree or position angle over a pulse feature (see Figures 2 and 3), simple Taylor-series expansions suffice:

$$
\begin{aligned}
p_L(\varphi) &= p_L(\varphi_0) + p'_L(\varphi_0)(\varphi − \varphi_0) + \frac{1}{2} p''_L(\varphi_0)(\varphi − \varphi_0)^2 + \cdots \\
&\equiv p_{L0} + p'_{L0}(\varphi − \varphi_0) + \frac{1}{2} p''_{L0}(\varphi − \varphi_0)^2 + \cdots; \quad \text{(A2)}
\end{aligned}
$$

$$
\begin{aligned}
\psi(\varphi) &= \psi(\varphi_0) + \psi'(\varphi_0)(\varphi − \varphi_0) + \frac{1}{2} \psi''(\varphi_0)(\varphi − \varphi_0)^2 + \cdots \\
&\equiv \psi_0 + \psi'_0(\varphi − \varphi_0) + \frac{1}{2} \psi''_0(\varphi − \varphi_0)^2 + \cdots; \quad \text{(A3)}
\end{aligned}
$$

$$
\begin{aligned}
p_C(\varphi) &= p_C(\varphi_0) + p'_C(\varphi_0)(\varphi − \varphi_0) + \frac{1}{2} p''_C(\varphi_0)(\varphi − \varphi_0)^2 + \cdots \\
&\equiv p_{C0} + p'_{C0}(\varphi − \varphi_0) + \frac{1}{2} p''_{C0}(\varphi − \varphi_0)^2 + \cdots. \quad \text{(A4)}
\end{aligned}
$$

To parameterize the pulse profile, we use a Gaussian (Appendix A.2) for each pulse feature (MP, IP, or LFC) or multiple Gaussians (Appendix A.3) for the MP.
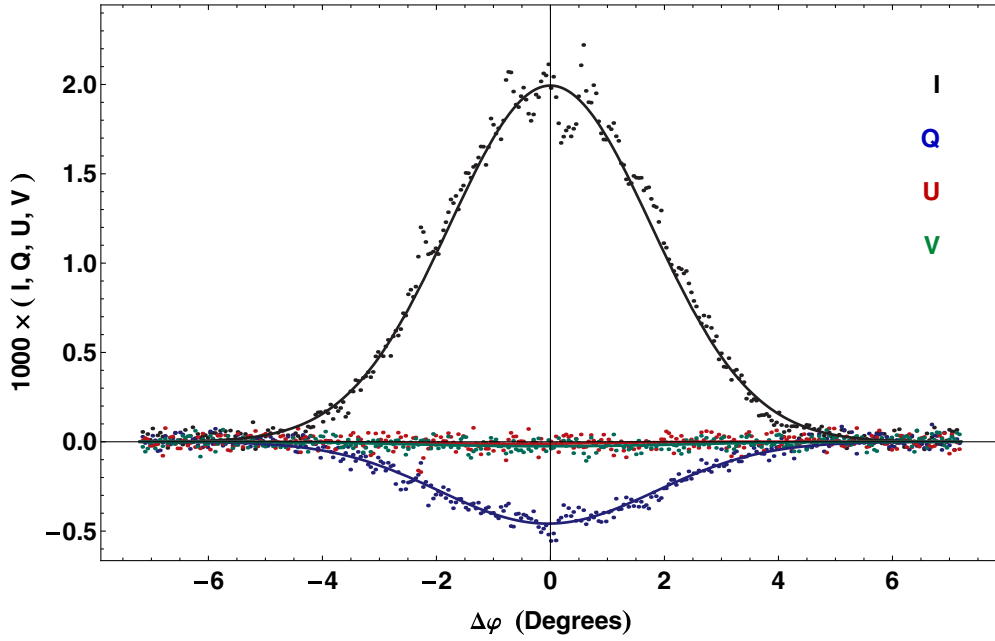
---

[7] http://reference.wolfram.com/mathematica/ref/NonlinearModelFit.html

Figure 7. Stokes data I, Q, U, and V vs. pulse phase offset $\Delta\varphi$ from the center of the main pulse (MP). The lines represent the best-fit (minimum-χ^2) Stokes functions for a single-Gaussian profile and up-to-second-order variations in the polarization degree and in position angle.

A.2. Single-Gaussian Fits to the MP, the IP, and to the LFC

To complete the parameterized model for the four Stokes functions, we assume a Gaussian profile:

$$I(\varphi) = I_0 \exp\left(-\frac{(\varphi - \varphi_0)^2}{2\sigma_\varphi^2}\right), \qquad (A5)$$

with I_0 the value of $I(\varphi)$ at pulse center, σ_φ the Gaussian width, and φ_0 the phase at the pulse center. Combining this parameterization with Equations (4), (5), (6), (A2), (A3), (A4), the full model for the other three Stokes functions follows:

$$
\begin{aligned}
Q(\varphi) = {} & I_0 \exp\left(-\frac{(\varphi - \varphi_0)^2}{2\sigma_\varphi^2}\right) \\
& \times \left[p_{L0} + p'_{L0}(\varphi - \varphi_0) + \frac{1}{2}p''_{L0}(\varphi - \varphi_0)^2\right] \\
& \times \cos\left(2\left[\psi_0 + \psi'_0(\varphi - \varphi_0) + \frac{1}{2}\psi''_0(\varphi - \varphi_0)^2\right]\right); \quad (A6)
\end{aligned}
$$

$$
\begin{aligned}
U(\varphi) = {} & I_0 \exp\left(-\frac{(\varphi - \varphi_0)^2}{2\sigma_\varphi^2}\right) \\
& \times \left[p_{L0} + p'_{L0}(\varphi - \varphi_0) + \frac{1}{2}p''_{L0}(\varphi - \varphi_0)^2\right] \\
& \times \sin\left(2\left[\psi_0 + \psi'_0(\varphi - \varphi_0) + \frac{1}{2}\psi''_0(\varphi - \varphi_0)^2\right]\right); \quad (A7)
\end{aligned}
$$

$$
\begin{aligned}
V(\varphi) = {} & I_0 \exp\left(-\frac{(\varphi - \varphi_0)^2}{2\sigma_\varphi^2}\right) \\
& \times \left[p_{C0} + p'_{C0}(\varphi - \varphi_0) + \frac{1}{2}p''_{C0}(\varphi - \varphi_0)^2\right]. \quad (A8)
\end{aligned}
$$

Figures 7–9 display Stokes data for the MP, IP, and LFC, respectively. The lines represent best-fit (minimum-χ^2) Stokes functions (Equations (A5), (A6), (A7), and (A8)) for a single-Gaussian profile $I(\varphi)$ and up-to-quadratic variations in linear-polarization degree $p_L(\varphi)$, in position angle $\psi(\varphi)$, and in circular-polarization degree $p_C(\varphi)$. Tables 2–4 tabulate the results of the χ^2 analysis for a Gaussian profile and retaining polarization terms (Equations (A6), (A7), and (A8)) through, zeroth, first, and second order, respectively. For each pulse feature—MP, IP, and LFC—the tables list the minimum χ^2 and degrees of freedom ν for I, Q, U, and V data sets combined and separately, followed by best-fit estimators and (1-sigma) uncertainties for the three pulse-profile parameters (I_0, σ_φ, φ_0) and for the relevant polarization coefficients (p_{L0}, p'_{L0}, p''_{L0}; ψ_0, ψ'_0, ψ''_0; p_{C0}, p'_{C0}, p''_{C0}). Note that these tables reference the pulse-phase angles (φ_0) and polarization position angles (ψ_0) to the MP, as we set $\varphi_{\mathrm{MP}} \equiv 0$ and were unable to obtain an absolute measurement of position angle ψ_{MP}.

Table 3 documents that, to within statistical uncertainties, $p'_{L0} = 0$, $\psi'_0 = 0$, and $p'_{C0} = 0$ for each of the three pulse features—MP, IP, or LFC. Equivalently, including the three linear coefficients $p'_{L0} = 0$, $\psi'_0 = 0$, and $p'_{C0} = 0$, does not result in a statistically significant reduction in the value of $\chi^2_{\min}$ (see Tables 2 and 3). In contrast, including the quadratic parameter p''_{L0} does significantly reduce the value of $\chi^2_{\min}$ for the MP (see Table 4 with Table 3 or 2), but not for the IP nor for the LFC.

A.3. Comparison of Model Fits to MP

Table 2 shows that a single-Gaussian profile and constant polarization degree and position angle provide a statistically adequate fit to the Stokes data for the IP and for the LFC. However, the simple model does not provide a statistically adequate fit to the Stokes data for the MP, at least in part due to the higher signal-to-noise ratio in the MP Stokes data. Consequently, here we investigate more complicated models in order to improve the goodness of the χ^2 fits to the MP Stokes data. In particular, we investigate using a multi-Gaussian function for the MP pulse profile. Table 5 lists the minimum χ^2
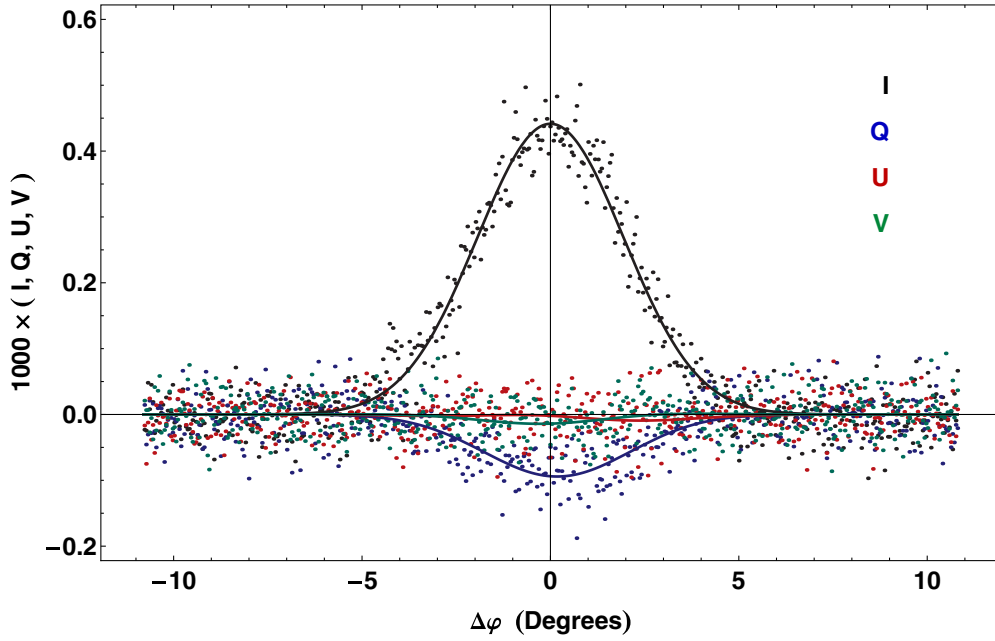
Figure 8. Stokes data I, Q, U, and V vs. pulse phase offset $\Delta\varphi$ from the center of the inter pulse (IP). The lines represent the best-fit (minimum-χ^2) Stokes functions for a single-Gaussian profile and up-to-second-order variations in polarization degree and in position angle.

Figure 9. Stokes data I, Q, U, and V vs. pulse phase offset $\Delta\varphi$ from the center of the low-frequency component (LFC). The lines represent the best-fit (minimum-χ^2) Stokes functions for a single-Gaussian profile and up-to-second-order variations in polarization degree and in position angle.
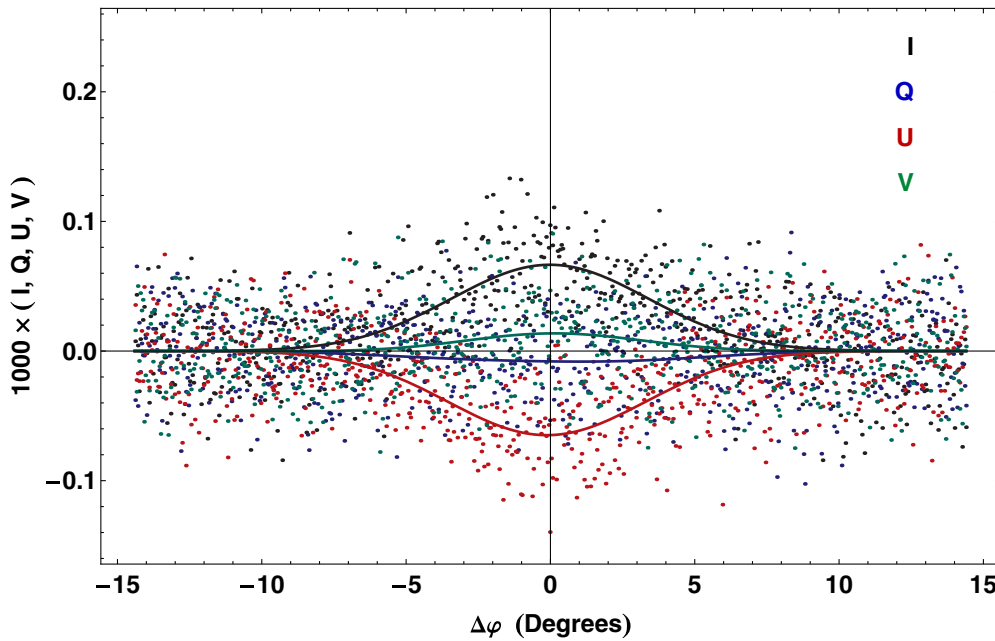
and degrees of freedom ν for I, Q, U, and V data sets combined and separately, followed by best-fit estimators and (1-sigma) uncertainties for the nine polarization coefficients (p_{L0}, p'_{L0}, p''_{L0}; ψ_0, ψ'_0, ψ''_0; p_{C0}, p'_{C0}, p''_{C0}) of the Taylor expansion through second order.

Comparison of the column "MP" in Table 3 with that in Table 4 (or, equivalently, with the column "1 Gaussian" in Table 5) finds that the inclusion of the three quadratic polarization coefficients—especially p''_{L0}—reduces χ^2_Q by 42 (from 473 to 431). While $\psi''_0 = 0$ and $p''_{C0} = 0$ within statistical uncertainties, $p''_{L0} \approx (0.9 \pm 0.2)\%/^\circ/^\circ$ is statistically significant but small.

The main cause of the poor fit of the 1 Gaussian model to the MP data, however, has nothing to do with polarization. Figure 4 illustrates that, for the fine time resolution and the high signal-to-noise ratio of the MP data, substructure in the pulse profile is quite evident. Using a 6 Gaussian (2 broad and 4 narrow) profile for $I(\varphi)$ substantially improves the fit. Comparing the column "6 Gaussian" with "1 Gaussian" in Table 5 finds that inclusion of $15 = 5 \times 3$ additional (Gaussian) parameters reduces χ^2_I by 1221 (from 1909 to 688). Even so, the fit to the Stokes data is not formally acceptable.

It is important to note that the best-fit expectation values and uncertainties for the polarization coefficients (p_{L0}, p'_{L0}, p''_{L0}; ψ_0,

Table 2
Best-fit Parameters for the MP, IP, and the LFC, Using a Simple Gaussian
for Each Profile and No Variations in Polarization Functions
$p_L(\varphi)$, $\psi(\varphi)$, and $p_C(\varphi)$

Parameter	Units	MP	IP	LFC
χ^2/ν		3081./1302	2022./1962	2518./2618
χ^2_I/ν_I		1910./324	561./489	577./653
χ^2_Q/ν_Q		460./322	534./487	674./651
χ^2_U/ν_U		441./322	463./487	603./651
χ^2_V/ν_V		269./323	463./488	664./652
I_0	×1000	1.9894 ± 0.0046	0.4414 ± 0.0044	0.0668 ± 0.0031
σ_φ	°	1.7801 ± 0.0047	1.947 ± 0.022	3.40 ± 0.14
$\varphi_0 - \varphi_{MP}$	°	≡ 0	145.399 ± 0.023	−37.79 ± 0.14
p_{L0}	%	23.67 ± 0.19	21.24 ± 0.81	98.3 ± 5.7
$\psi_0 - \psi_{MP}$	°PA	≡ 0	1.0 ± 1.1	40.3 ± 1.2
p_{C0}	%	−1.40 ± 0.18	−2.70 ± 0.78	19.0 ± 4.0

Table 3
Best-fit Parameters for the MP, the IP, and the LFC, Using a Simple Gaussian for Each Profile and Up-to-linear
Variations in Polarization Functions $p_L(\varphi)$, $\psi(\varphi)$, and $p_C(\varphi)$

Parameter	Units	MP	IP	LFC
χ^2/ν		3076./1299	2017./1959	2517./2615
χ^2_I/ν_I		1910./324	561./489	577./653
χ^2_Q/ν_Q		456./320	532./485	674./649
χ^2_U/ν_U		440./320	462./485	602./649
χ^2_V/ν_V		269./322	463./487	664./651
I_0	×1000	1.9894 ± 0.0046	0.4415 ± 0.0044	0.0668 ± 0.0031
σ_φ	°	1.7801 ± 0.0047	1.946 ± 0.022	3.40 ± 0.14
$\varphi_0 - \varphi_{MP}$	°	≡ 0	145.389 ± 0.023	−37.74 ± 0.20
p_{L0}	%	23.67 ± 0.19	21.25 ± 0.81	98.3 ± 5.7
p'_{L0}	%/°	−0.32 ± 0.15	1.09 ± 0.59	− 0.9 ± 2.4
$\psi_0 - \psi_{MP}$	°PA	≡ 0	0.9 ± 1.1	40.3 ± 1.2
ψ'_0	°PA/°	−0.15 ± 0.18	0.91 ± 0.78	−0.18 ± 0.48
p_{C0}	%	−1.40 ± 0.18	−2.70 ± 0.78	19.0 ± 4.0
p'_{C0}	%/°	−0.01 ± 0.14	0.38 ± 0.57	0.3 ± 1.7

Table 4
Best-fit Parameters for the MP, for the IP, and for the LFC, Using a Simple Gaussian for Each
Profile and Up-to-quadratic Variations in Polarization Functions $p_L(\varphi)$, $\psi(\varphi)$, and $p_C(\varphi)$

Parameter	Units	MP	IP	LFC
χ^2/ν		3049./1296	2016./1956	2517./2612
χ^2_I/ν_I		1909./324	561./489	577./653
χ^2_Q/ν_Q		432./318	531./483	674./647
χ^2_U/ν_U		440./318	461./483	603./647
χ^2_V/ν_V		268./321	462./486	664./650
I_0	×1000	1.9927 ± 0.0047	0.4414 ± 0.0045	0.0666 ± 0.0034
σ_φ	°	1.7742 ± 0.0048	1.947 ± 0.023	3.42 ± 0.20
$\varphi_0 - \varphi_{MP}$	°	≡ 0	145.389 ± 0.023	−37.75 ± 0.20
p_{L0}	%	22.99 ± 0.23	21.24 ± 0.99	98.1 ± 7.0
p'_{L0}	%/°	−0.32 ± 0.15	1.03 ± 0.59	−0.9 ± 2.4
p''_{L0}	%/°/°	0.86 ± 0.17	−0.04 ± 0.61	0.1 ± 1.4
$\psi_0 - \psi_{MP}$	°PA	≡ 0	−0.1 ± 1.3	40.8 ± 1.4
ψ'_0	°PA/°	−0.16 ± 0.17	0.82 ± 0.79	−0.16 ± 0.48
ψ''_0	°PA/°/°	−0.06 ± 0.18	1.07 ± 0.80	−0.21 ± 0.28
p_{C0}	%	−1.25 ± 0.22	−3.15 ± 0.96	20.5 ± 4.9
p'_{C0}	%/°	0.01 ± 0.15	0.38 ± 0.57	0.3 ± 1.7
p''_{C0}	%/°/°	−0.20 ± 0.16	0.47 ± 0.59	−0.49 ± 0.96

ψ'_0, ψ''_0; p_{C0}, p'_{C0}, p''_{C0}) are rather insensitive to details of the pulse profile. Thus, we compensate for fine substructure in the pulse profile by increasing the estimators for the measurement standard deviations until a statistically acceptable fit is achieved.

That is, we adjust σ_I, σ_Q, σ_U, and σ_V until (Equation (A1)) χ^2_I/ν_I, χ^2_Q/ν_Q, χ^2_U/ν_U, and χ^2_V/ν_V, respectively, are close to unity. The column "1 Gaussian (Adj.)" in Table 5 shows the best-fit polarization parameters for a single-Gaussian profile, with

Table 5
Comparison of Results of Fitting the Main Pulse (MP) Profile with a Simple Gaussian, with a Multi-Gaussian, and with a Simple Gaussian after Adjusting Weightings

Parameter	Units	1-Gaussian	6-Gaussian	1-Gaussian (Adj.)
χ^2/ν		3049./1296	1823./1281	1281./1296
χ^2_I/ν_I		1909./324	688./309	324./324
χ^2_Q/ν_Q		432./318	430./303	318./318
χ^2_U/ν_U		440./318	438./303	318./318
χ^2_V/ν_V		268./321	267./306	321./321
p_{L0}	%	22.99 ± 0.23	22.91 ± 0.24	22.98 ± 0.30
p'_{L0}	%/°	-0.32 ± 0.15	-0.29 ± 0.15	-0.31 ± 0.19
p''_{L0}	%/°/°	0.86 ± 0.17	0.89 ± 0.19	0.88 ± 0.22
ψ_0	°PA	-89.34 ± 0.27	-89.38 ± 0.29	-89.34 ± 0.32
ψ'_0	°PA/°	-0.16 ± 0.17	-0.19 ± 0.17	-0.16 ± 0.20
ψ''_0	°PA/°/°	-0.06 ± 0.18	0.05 ± 0.20	-0.06 ± 0.21
p_{C0}	%	-1.25 ± 0.22	-1.27 ± 0.23	-1.25 ± 0.20
p'_{C0}	%/°	-0.01 ± 0.15	-0.02 ± 0.14	-0.01 ± 0.13
p''_{C0}	%/°/°	-0.20 ± 0.16	-0.18 ± 0.18	-0.20 ± 0.15

Note. The models retain up-to-quadratic variations in the polarization functions $p_L(\varphi)$, $\psi(\varphi)$, and $p_C(\varphi)$.

weightings adjusted as described. The only noticeable effect of this adjustment upon the best-fit polarization parameters is a small change—typically an increase—in their uncertainties. The uncertainties quoted in Table 1 (Section 3) are the typically more conservative values obtained using the single-Gaussian profiles and adjusted weightings.

REFERENCES

Abdo, A. A., Ajello, M., Allafort, A., et al. 2013, ApJS, 208, 17
Abdo, A. A., Allen, B. T., Atkins, R., et al. 2012, ApJ, 750, 63
Aharonian, F., Akhperjanian, A. G., Bazer-Bachi, A. R., et al. 2006, A&A, 457, 899
Aharonian, F., Akhperjanian, A., Beilicke, M., et al. 2004, ApJ, 614, 897
Aleksić, J., Alvarez, E. A., Antonelli, L. A., et al. 2012, A&A, 540, A69
Aliu, E., Arlen, T., Aune, T., et al. 2011, Sci, 334, 69
Allen, B. T., & Yodh, G. B. 2007, in AIP Conf. Ser. 921, The First Glast Symposium, ed. B. T. Allen & G. B. Yodh (Melville, NY: AIP), 528
Backer, D. C., Wong, T., & Valanju, J. 2000, ApJ, 543, 740
Bai, N., & Spitkovsky, A. 2010, ApJ, 715, 1282
Bhat, N. D. R., Tingay, S. J., & Knight, H. S. 2008, ApJ, 676, 1200
Blaskiewicz, M., Cordes, J. M., & Wasserman, I. 1991, ApJ, 370, 643
Bridle, A. H. 1970, Natur, 225, 1035
Bühler, R., & Blandford, R. 2014, RPPh, 77, 066901
Contopoulos, I., & Kalapotharakos, C. 2010, MNRAS, 404, 767
Deutsch, A. J. 1955, AnAp, 18, 1
Dyks, J., Harding, A. K., & Rudak, B. 2004, ApJ, 606, 1125
Dyks, J., & Rudak, B. 2003, ApJ, 598, 1201
Espinoza, C. M., Guillemot, L., Çelik, Ö., et al. 2013, MNRAS, 430, 571
Forot, M., Laurent, P., Grenier, I. A., Gouiffès, C., & Lebrun, F. 2008, ApJL, 688, L29
Gould, D. M., & Lyne, A. G. 1998, MNRAS, 301, 235
Hankins, T. H., Kern, J. S., Weatherall, J. C., & Eilek, J. A. 2003, Natur, 422, 141
Harding, A. K., DeCesar, M. E., Miller, M. C., Kalapotharakos, C., & Contopoulos, I. 2011, in Proc. of 2011 Fermi Symposium, eConf C110509, (arXiv:1111.0828)
Hibschman, J. A., & Arons, J. 2001, ApJ, 546, 382
Jones, D. H. P., Smith, F. G., & Wallace, P. T. 1981, MNRAS, 196, 943

Kalapotharakos, C., Kazanas, D., Harding, A., & Contopoulos, I. 2012, ApJ, 749, 2
Karastergiou, A., & Johnston, S. 2006, MNRAS, 365, 353
Karuppusamy, R., Stappers, B., & van Straten, W. 2008, PASP, 120, 191
Karuppusamy, R., Stappers, B. W., & van Straten, W. 2010, A&A, 515, A36
Kuiper, L., Hermsen, W., Cusumano, G., et al. 2001, A&A, 378, 918
Kuzmin, A., Losovsky, B. Y., Jordan, C. A., & Smith, F. G. 2008, A&A, 483, 13
Li, J., Spitkovsky, A., & Tchekhovskoy, A. 2012, ApJ, 746, 60
Lyne, A., Graham-Smith, F., Weltevrede, P., et al. 2013, Sci, 342, 598
Lyne, A. G., & Graham-Smith, F. 2006, Pulsar Astronomy (3rd ed.; Cambridge: Cambridge Univ. Press)
Majid, W. A., Naudet, C. J., Lowe, S. T., & Kuiper, T. B. H. 2011, ApJ, 741, 53
Manchester, R. N. 1971, ApJS, 23, 283
Manchester, R. N., Hobbs, G. B., Teoh, A., & Hobbs, M. 2005, AJ, 129, 1993
Moffett, D. A., & Hankins, T. H. 1996, ApJ, 468, 779
Moffett, D. A., & Hankins, T. H. 1999, ApJ, 522, 1046
Moran, P., Shearer, A., Gouiffès, C., & Laurent, P. 2013a, arXiv:1302.3622
Moran, P., Shearer, A., Mignani, R. P., et al. 2013b, MNRAS, 433, 2564
Muslimov, A. G., & Harding, A. K. 2004, ApJ, 606, 1143
Ng, C.-Y., & Romani, R. W. 2008, ApJ, 673, 411
Oort, J. H., & Walraven, T. 1956, BAN, 12, 285
Pétri, J., & Kirk, J. G. 2005, ApJL, 627, L37
Pierbattista, M., et al. 2014, A&A, submitted (arXiv:1403.3849)
Radhakrishnan, V., & Cooke, D. J. 1969, ApL, 3, 225
Rankin, J. M. 1990, ApJ, 352, 247
Romani, R. W., & Watters, K. P. 2010, ApJ, 714, 810
Romani, R. W., & Yadigaroglu, I.-A. 1995, ApJ, 438, 314
Silver, E. H., Kestenbaum, H. L., Long, K. S., et al. 1978, ApJ, 225, 221
Słowikowska, A., Kanbach, G., Kramer, M., & Stefanescu, A. 2009, MNRAS, 397, 103
Smith, F. G., Jones, D. H. P., Dick, J. S. B., & Pike, C. D. 1988, MNRAS, 233, 305
van Straten, W., & Bailes, M. 2011, PASA, 28, 1
van Straten, W., Demorest, P., & Oslowski, S. 2012, Astron. Res. Technol., 9, 237
Venter, C., Johnson, T. J., & Harding, A. K. 2012, ApJ, 744, 34
Weltevrede, P., & Johnston, S. 2008, MNRAS, 391, 1210
Wolfram Research, Inc. 2013, Mathematica, Version 9.0 (Champaign, IL: Wolfram Research)
Woltjer, L. 1957, BAN, 13, 301